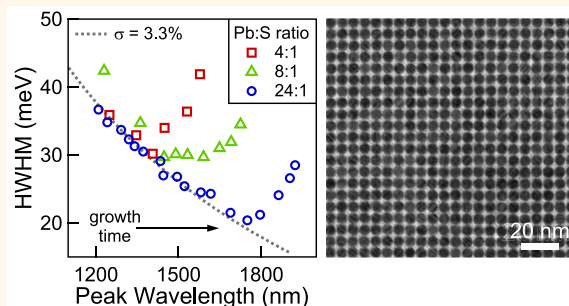


# Monodisperse, Air-Stable PbS Nanocrystals *via* Precursor Stoichiometry Control

Mark C. Weidman, Megan E. Beck, Rachel S. Hoffman, Ferry Prins, and William A. Tisdale\*

Department of Chemical Engineering, Massachusetts Institute of Technology, Cambridge, Massachusetts 02139, United States

**ABSTRACT** Despite their technological importance, lead sulfide (PbS) nanocrystals have lagged behind nanocrystals of cadmium selenide (CdSe) and lead selenide (PbSe) in terms of size and energy homogeneity. Here, we show that the ratio of lead to sulfur precursor available during nucleation is a critical parameter affecting subsequent growth and monodispersity of PbS nanocrystal ensembles. Applying this knowledge, we synthesize highly monodisperse (size dispersity <5%) PbS nanocrystals over a wide range of sizes (exciton energies from 0.70 to 1.25 eV, or 1000–1800 nm) without the use of size-selective precipitations. This degree of monodispersity results in absorption peak half width at half max (HWHM) values as small as 20 meV, indicating an ensemble that is close to the homogeneous limit. Photoluminescence emission is correspondingly narrow and exhibits small Stokes shifts and quantum efficiencies of 30–60%. The nanocrystals readily self-assemble into ordered superlattices and exhibit exceptional air stability over several months.



**KEYWORDS:** lead sulfide · PbS · quantum dot · nanocrystal · monodisperse · infrared photoluminescence · self-assembly · lead chloride

Lead sulfide (PbS) nanocrystals, also called quantum dots (QDs), have a size-dependent, tunable near-infrared band gap which makes them particularly interesting for photovoltaics,<sup>1–3</sup> photodetectors,<sup>3,4</sup> and infrared light emission.<sup>5</sup> In most of these applications, it is desirable to have monodisperse QDs, that is, nanocrystals of nearly all the same size. For photovoltaics, monodispersity creates a flat energy landscape, which should maximize the rate at which charge carriers can be extracted from the QD film.<sup>6</sup> Furthermore, simulations suggest that having the narrow energy distribution imparted by monodispersity is key for maximizing the open-circuit voltage in these devices.<sup>6,7</sup> Monodispersity is also critical for the formation of nanocrystal superlattices.<sup>8</sup> Such ordered arrangements of nanocrystals increase the packing fraction (better light absorption per volume) and can enhance inter-dot coupling to increase the potential for band-like transport.<sup>6,9,10</sup> For infrared photodetection and emission, monodispersity provides narrow and well-controlled absorption and emission. In their visible light

counterparts, narrow emission line width has emerged as an essential characteristic for commercial viability.<sup>11</sup> Lastly, having QDs of all the same size and energy facilitates fundamental studies of QD excitonic structure and photophysical processes such as multiple exciton generation (MEG)<sup>12</sup> and hot electron transfer.<sup>13</sup>

Despite the benefits offered by monodisperse nanocrystal ensembles, current synthetic methods for PbS QDs<sup>14–16</sup> have lagged behind those for cadmium selenide (CdSe)<sup>17–21</sup> and lead selenide (PbSe)<sup>22–25</sup> in terms of the monodispersity achievable over a wide range of band gaps. While the band gaps of PbS and PbSe QDs can be tuned over similar ranges, PbS offers unique advantages over PbSe in optoelectronic devices, such as improved air stability<sup>16</sup> and the higher abundance/lower cost of sulfur as compared to selenium.<sup>26</sup> Further, PbS is consistently the highest-performing material used in QD solar cells.<sup>1,12,27,28</sup>

Here, we show that the initial ratio of lead to sulfur precursor strongly influences the growth and monodispersity of PbS

\* Address correspondence to tisdale@mit.edu.

Received for review April 4, 2014 and accepted May 19, 2014.

Published online May 19, 2014 10.1021/nn5018654

© 2014 American Chemical Society

nanocrystals. For the prototypical reaction of  $\text{PbCl}_2$  with sulfur in oleylamine,<sup>15,16</sup> we find that a large excess of lead precursor results in the formation of fewer nuclei and extends the period of growth by monomer addition from solution. By increasing the Pb:S precursor ratio to as much as 24:1, we were able to delay the onset of Ostwald ripening for up to 6 h, making it possible to synthesize monodisperse PbS QDs having peak absorption over a range of 1000–1800 nm (1.25–0.70 eV, 4.3–8.4 nm diameter) and size dispersities of 3–5%, without performing size-selective precipitations. We have also developed an effective purification method, such that excess lead precursor in the reaction product can be completely removed quickly and efficiently. Due to the unprecedented monodispersity of these nanocrystals, the half width at half max (HWHM) of the first absorption peak reaches values as small as 20 meV, suggesting a QD ensemble that is almost entirely homogeneously broadened. The QDs have correspondingly narrow emission peaks and small Stokes shifts. The QDs also exhibit exceptional air stability, as evidenced by high quantum yield and unchanging absorption spectra when stored in air for several months.

## RESULTS AND DISCUSSION

To determine the effect of Pb:S precursor ratio on nanocrystal growth, PbS QDs were synthesized at 120 °C with Pb:S precursor ratios of 4:1, 8:1, and 24:1. After injection of the sulfur solution into the lead solution, growth was allowed to occur at 120 °C for several hours. During this time, the QDs increased in size and the first absorption peak shifted to longer wavelengths. In this work, we use the HWHM of the first absorption peak as a metric for the size dispersity of the QDs, with a small HWHM value signaling a monodisperse batch of nanocrystals. The HWHM is determined from the peak absorption to the half max value at longer wavelength (*i.e.*, to the right of the first absorption peaks shown in Figure 1).

To illustrate that HWHM is a reliable metric for dispersity, we compare in Figure 1 the absorption spectra of QDs synthesized with the same first absorption peak location, but different peak HWHM values. The spectrum shown in red has a HWHM of 42 meV, whereas the blue spectrum has a HWHM of only 25 meV. We can identify five absorption features in the blue spectrum (determined by taking the second derivative of the data, not shown), whereas only two absorption features are observed in the red spectrum. The transmission electron microscopy (TEM) images of these samples confirm the improved monodispersity of the 25 meV HWHM sample over the 42 meV sample, as well as the ability to self-assemble, which is lacking in the 42 meV sample.

In Figure 2, we plot the HWHM for QDs synthesized with varying Pb:S precursor ratios as a function of their

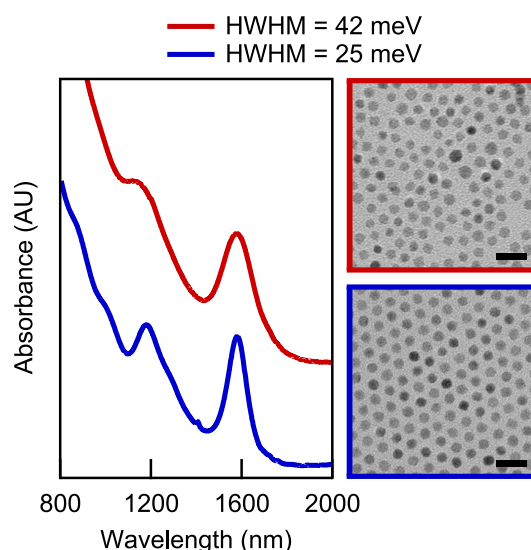


**Figure 1.** Comparison of absorption spectra and TEM micrographs for QDs having the same peak absorption wavelength but different HWHM values. TEM scale bars are 20 nm.

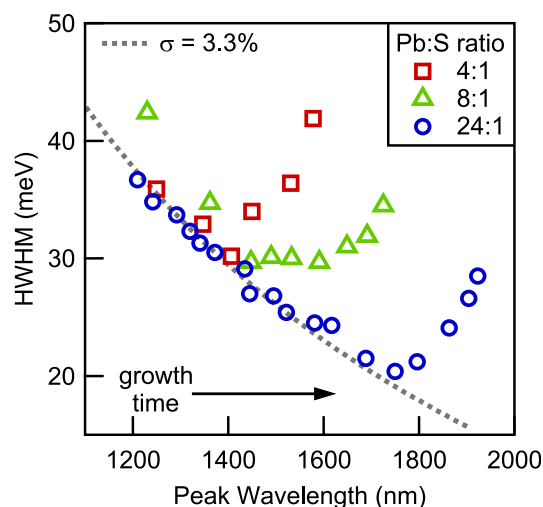


**Figure 2.** Half width at half-maximum (HWHM) of the first absorption peak plotted versus peak wavelength for different Pb:S precursor ratios. All syntheses were performed at a reaction temperature of 120 °C. The dashed gray line is the expected trend for a QD dispersion having 3.3% size dispersity.

peak absorption wavelength. We include the smallest HWHM values obtained for at least two syntheses at each precursor ratio studied. The dashed gray line is the expected trend for a QD dispersion having 3.3% size dispersity (see further discussion below). For a 4:1 precursor ratio, the HWHM followed the line of constant monodispersity until growth reached a peak wavelength value near 1400 nm, at which point HWHM began to increase rapidly. With an 8:1 Pb:S ratio, the monodisperse growth occurred until about 1600 nm, at which point HWHM started to increase with increasing absorption wavelength. For a ratio of 24:1, the monodisperse growth proceeded up to 1800 nm, and reached values as low as 20 meV. Interestingly, a

precursor ratio of 24:3 resulted in a growth curve similar to 8:1 (see Figure S8), indicating that it is precursor *ratio*, rather than total precursor concentration, that enables monodisperse growth.

Elemental analysis by energy-dispersive X-ray spectroscopy (EDS) confirmed previous reports that PbS nanocrystals prepared by this reaction are lead-rich.<sup>15,16</sup> A comparison between the similarly sized nanocrystals shown in Figure 1, synthesized using 4:1 and 24:1 Pb:S ratios, revealed no statistically significant difference in their elemental composition (see Figure S14 and Table S1).

To investigate the growth mechanism, we monitored the amount of unreacted sulfur present in a 24:1 ratio synthesis by withdrawing aliquots as the reaction progressed. We then precipitated the QDs using oleic acid, leaving any unreacted sulfur in the supernate (see Figure S2). Qualitatively, we see that sulfur is consumed as the reaction proceeds, indicating that the monodisperse phase of nanocrystal growth proceeds by diffusion-limited monomer addition from solution,<sup>20,29,30</sup> as expected for this reaction.<sup>15</sup> The minimum in HWHM thus represents the point at which Ostwald ripening takes over as the dominant growth mechanism.

The delayed onset of Ostwald ripening under the condition of constant limiting reagent (sulfur) necessarily implies that, as the Pb:S precursor ratio is increased, fewer nanocrystal nuclei are formed during the initial nucleation burst. Precursor concentration has previously been used to control nucleation of CdS and CdSe nanocrystals, most notably by Abe *et al.*<sup>20</sup> However, these authors observed the opposite dependence on precursor ratio: larger stoichiometric excess (and larger overall precursor concentration) accelerated the nucleation rate, resulting in the formation of *more* nanocrystal nuclei and *shortening* the time during which nanocrystals grow *via* monomer addition.<sup>20</sup> This important difference indicates that precursor reaction rate is not the mechanism by which precursor stoichiometry affects nanocrystal growth in our PbS system. Instead, we speculate that the notable increase in solution viscosity, caused by larger quantities of PbCl<sub>2</sub>, decreases mass transfer in the system and leads to an overall reduction in nucleation events. Forming fewer nuclei leaves more sulfur monomer available to add to existing nuclei after the nucleation burst, and prolongs the time during which nanocrystals grow *via* monomer addition.

To test our understanding of the growth mechanism, we investigated the effects of adding additional sulfur precursor after the initial nucleation burst. We prepared an 8:1 reaction as described, then slowly added half the amount of sulfur used for the initial nucleation burst after the reaction had proceeded for 1 min. The additional sulfur delayed the onset of line width broadening, allowing growth to proceed along the line of constant monodispersity for longer times (see Figure S9). These observations confirm that the

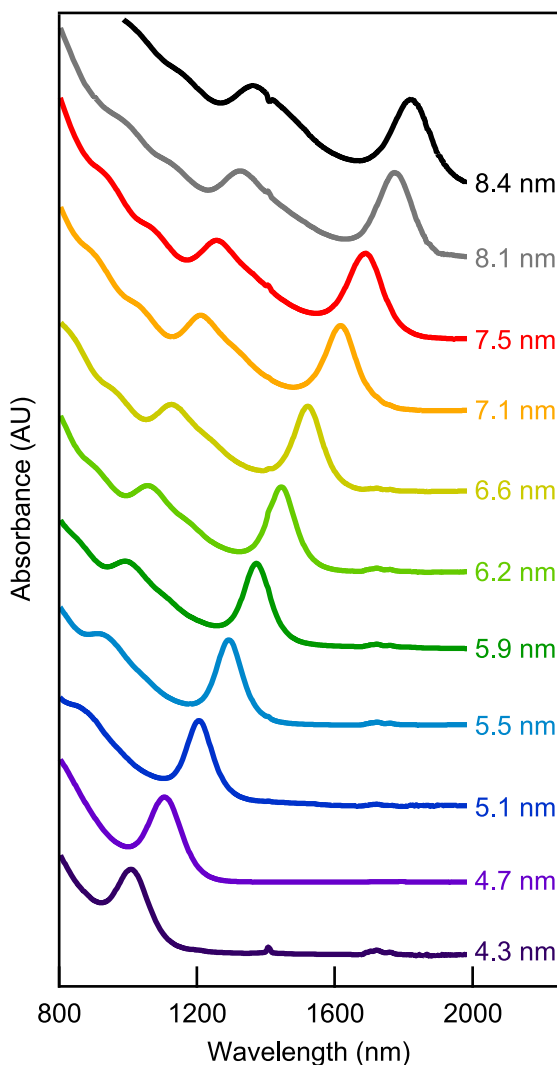


**Figure 3.** Absorption spectra using a 24:1 Pb:S precursor ratio showing the synthetic range of 1000–1800 nm (1.25–0.70 eV). The bottom two spectra (dark violet, purple) were synthesized at 40 and 80 °C, respectively, while all others were synthesized at 120 °C. Labels indicate the average diameter of the QDs, as determined by eq 2. Spectra are normalized to have the same peak amplitude and offset for clarity.

minimum in HWHM marks the end of the growth by monomer addition phase and the beginning of a growth phase dominated by Ostwald ripening, indicating that the growth mechanism in this reaction closely mimics that which has been studied for II–VI and III–V colloidal nanocrystals.<sup>30</sup> We find that the major role of the excess lead precursor is then to control the balance between precursors being consumed during nucleation and precursors being leftover to further grow nuclei. This insight into the growth mechanism could be used to design QD production processes that make more economical use of starting materials and maximize reaction yield.

For the remainder of this work, we focus on the properties of QDs produced using a 24:1 precursor ratio, as it most reliably produced monodisperse QDs

over the range of interest. However, we note that for short growth times, monodisperse QDs can be produced with Pb:S ratios of 4:1 or 8:1, increasing the yield per lead equivalent. The data in Figure 2 show that at a reaction temperature of 120 °C, the smallest QDs produced have a peak absorption near 1200 nm. To increase the synthetic range, particularly to access smaller sized QDs which are useful in photovoltaic applications, we decreased the reaction temperature to either 80 or 40 °C. These lower temperatures allowed us to access peak absorption in the 1000–1200 nm range, but resulted in slightly larger dispersity and less consistency. In Table 1, we suggest guidelines for accessing a desired peak absorption using our synthetic protocol (see Figure S4 for peak wavelength as a function of growth time and temperature).

Figure 3 contains select absorption spectra for the 24:1 synthesis method, normalized by peak amplitude and offset for clarity. The average QD diameter is indicated next to each curve. The overall range is 1000–1800 nm, or 1.25–0.70 eV. The two spectra at the bottom of Figure 3, shown in dark violet and purple, were synthesized at 40 and 80 °C, respectively. All other spectra were synthesized with a reaction temperature of 120 °C. In almost all spectra it is possible to see many higher energy absorption features. When plotted *versus* wavelength, the peaks appear to broaden at longer wavelengths, but energetically the peak widths are continuously decreasing (see Figure S3 for the same spectra plotted *versus* energy).

Purification of the QD product is a critical step to remove unreacted precursor materials as well as excess solvent. As seen in previous works using PbCl<sub>2</sub> as the lead precursor source,<sup>31–33</sup> a significant drawback of this method is the presence of unreacted PbCl<sub>2</sub> in the final product (see Figure S1). This PbCl<sub>2</sub> can remain in solution for weeks to months, especially when using the highly nonstoichiometric Pb:S precursor ratios employed here. These impurities would likely be detrimental to the performance of QD optoelectronic devices, so it is desirable to be able to quickly and effectively remove them. During the course of this work, we experimented with two different purification methods for removing excess precursors (see the Supporting Information for detailed procedures): precipitation with alcohols and precipitation with excess oleic acid.<sup>15</sup> All purification steps were performed under ambient conditions.

Traditional purification with butanol and methanol precipitated both the PbS QDs and unreacted PbCl<sub>2</sub>, making it difficult to separate these two components. We found that adequate purification using this method is possible, but that the QDs suspensions must be centrifuged frequently for weeks after synthesis until all the PbCl<sub>2</sub> has precipitated.

Unlike the alcohol antisolvents, oleic acid selectively precipitated the QDs, but not the unreacted PbCl<sub>2</sub>

**TABLE 1. Guidelines for PbS QD Synthesis**

peak absorption (nm)	temperature (°C)	growth time
975–1050	40	10 s to 5 m
1050–1200	80	10 s to 30 m
1200–1800	120	10 s to 6 h

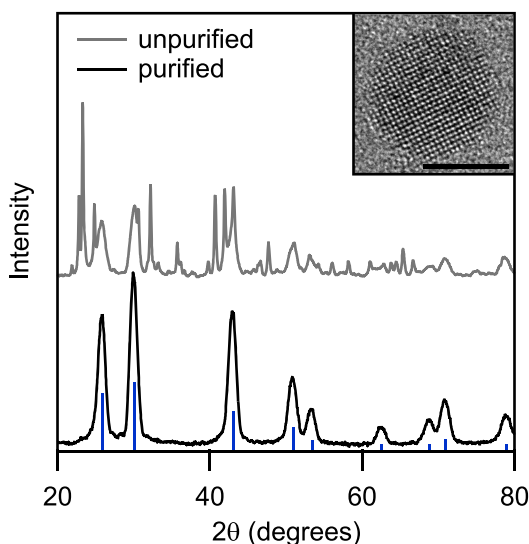


**Figure 4.** XRD on as-synthesized QDs before purification (gray, above) and following purification with oleic acid (black, below). The blue vertical bars are the reference PbS peak locations (ICDD PDF number 00-005-0592). Inset is HRTEM of a single PbS QD. Scalebar is 5 nm.

or sulfur. We found that the oleic acid precipitation could be performed repeatedly (more than 5 times) without compromising colloidal stability, indicating that the oleic acid precipitation does not significantly strip ligands off the surface of the QDs, as alcohol antisolvents have been shown to do after repeated exposure.<sup>15,34</sup> Typically, purification using oleic acid enabled complete PbCl<sub>2</sub> removal less than 24 h after synthesis (compared to ~4 weeks when using alcohols for purification).

In Figure 4, we show X-ray diffraction (XRD) patterns collected from the same batch of QDs, synthesized with a 24:1 Pb:S precursor ratio, before (gray) and after (black) purification with oleic acid as the antisolvent. The many additional peaks observed in the unpurified sample correspond to diffraction from crystalline PbCl<sub>2</sub>. The purified sample shows no peaks from crystalline PbCl<sub>2</sub> and only those expected for PbS. We found XRD to be the most effective technique for evaluating purity, and note that a relatively fast scan from 20 to 40° is sufficient to determine if purification is complete.

To further characterize our QDs, we used TEM and small-angle X-ray scattering (SAXS) to determine the average diameter of the QDs (see Figures S10 and S11 for typical data analysis). In total, 12 samples were analyzed using TEM and SAXS (10 of which were



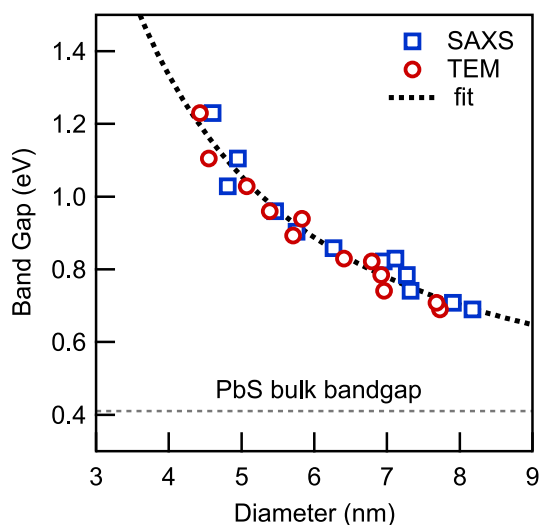


**Figure 5.** QD band gap versus diameter, as measured by TEM and SAXS. The best-fit curve (dotted line) is given by eq 2.

measured using both methods). In Figure 5, we plot the band gap of each QD versus its measured diameter. The data plotted in Figure 5 are available in Table S2.

We fit the data to an empirical equation of the form,

$$E_g = c + \frac{1}{ad^2 + bd} \quad (1)$$

where  $c$  is the bulk band gap of PbS (0.41 eV) and  $a$  and  $b$  are fitting parameters. The best-fit form is

$$E_g = 0.41 + \frac{1}{0.0392d^2 + 0.114d} \quad (2)$$

where  $E_g$  is expressed in electronvolts (eV) and the QD diameter  $d$  is expressed in nanometers.

When the empirically determined correlation between band gap and QD size is used, it is possible to relate the peak absorption HWHM to the size dispersity ( $\sigma$ ). To do this, we assume that the first absorption peak is Gaussian in form and that the absorption line shape for a single QD is a delta function. We note that this assumption leads to a systematic over-estimation of the size dispersity because we are not accounting for the homogeneous line width of a single PbS QD. In terms of the parameters defined in eq 1, one may derive an expression for the HWHM as a function of mean diameter,  $d$ , and size dispersity,  $\sigma$ ,

$$\text{HWHM}(d, \sigma) = \frac{\sigma(a\gamma^2 d\sigma + 2a\gamma d + b\gamma)}{(\gamma\sigma + 1)(ad + b)(a\gamma d\sigma + ad + b)d} \quad (3)$$

where  $a$  and  $b$  are the parameters determined earlier ( $a = 0.0392$ ,  $b = 0.114$ ) and  $\gamma$  converts standard deviation to the HWHM ( $\gamma = 1.177$ ). The standard deviation of the size distribution,  $\sigma$ , is normalized to  $d$  so that it is unitless and can easily be converted to a percentage of the mean diameter. Equation 3, with numerical values, is given in the Supporting Information.

The dotted line in Figure 2 is a plot of eq 3, using  $\sigma = 3.3\%$ . We see that the HWHM is decreasing as the

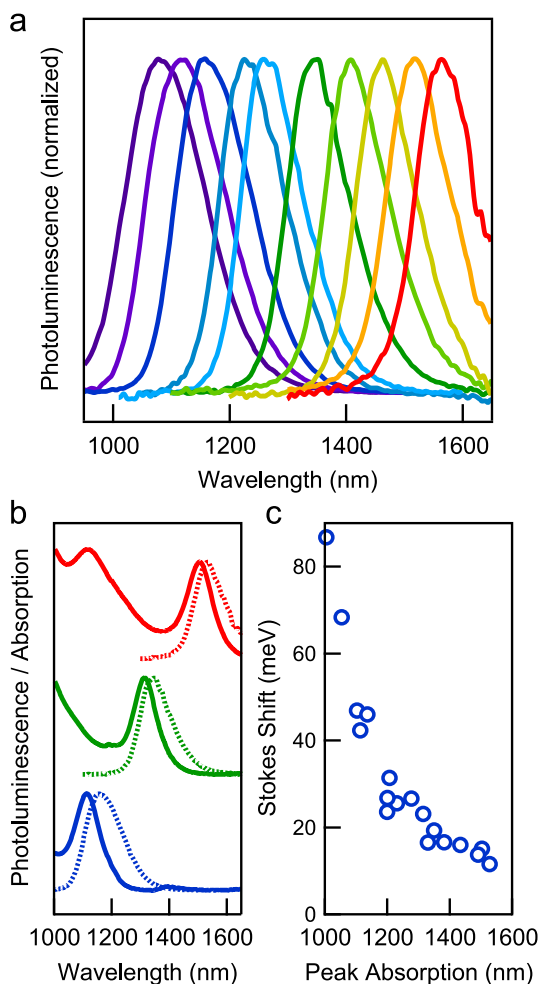


**Figure 6.** (a) Photoluminescence spectra for QDs dispersed in tetrachloroethylene. (b) Comparison of absorption spectra (solid lines) and photoluminescence spectra (dashed lines), normalized for constant peak intensity. (c) Stokes shift plotted as a function of peak absorption wavelength.

peak wavelength is increasing. This trend is expected due to the nonlinear relationship between band gap and nanocrystal size. For a fixed value of dispersity, the HWHM increases as the diameter of the QDs decreases because the band gap is more sensitive to QD size for small QDs than for large QDs. Thus, the HWHM is not an absolute measure of dispersity but instead depends on the diameter of the QDs.

In addition to showing narrow absorption line width, the QDs synthesized here also exhibit bright and spectrally narrow infrared luminescence, with photoluminescence quantum efficiency typically in the range of 30–60%. In Figure 6a, we present photoluminescence spectra collected from ten different QD sizes. Tunable emission spans the range of 1080–1560 nm, with 1600 nm being the upper limit of the detector used in this study. In Figure 6b, we plot both the absorption and emission spectra for three different sizes of QDs to show that emission has similarly narrow line width as compared to absorption (see Figure S6 for a graphical comparison) and that Stokes shift is minimal.

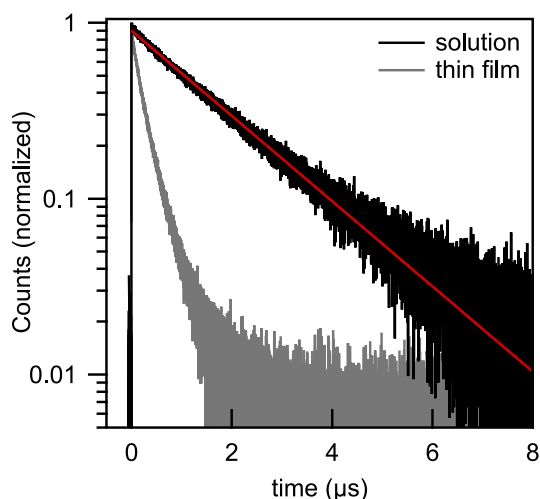


**Figure 7.** Photoluminescence lifetime measurements for QDs dispersed in TCE and drop cast into a thin film. An exponential fit to the solution data gives a lifetime of  $1.8 \mu\text{s}$ . The  $1/e$  lifetime of the thin film is 260 ns.

In Figure 6c, we show the measured Stokes shift as a function of the peak absorption wavelength, which approaches values as small as 10 meV.

We measured the photoluminescence lifetime of our QDs in thin film and solution using time correlated single photon counting. The photoluminescence lifetime measurements are shown in Figure 7. The solution phase measurements are fit well by a single exponential decay with a lifetime of  $1.8 \mu\text{s}$ . When the same QDs are dropcast into a thin film, with native oleic acid ligands, the photoluminescence decay is no longer single exponential. In thin film, the  $1/e$  lifetime is approximately 260 ns. The single-exponential decay of the solution photoluminescence indicates homogeneity of the nanocrystal dispersion. The comparatively short lifetime in the dropcast film may be indicative of efficient exciton diffusion or exciton dissociation.<sup>35,36</sup>

The QDs synthesized using the recipe developed here show air stability after being stored as a dry powder in laboratory air for several months. In Figure 8, we compare the absorption spectra for three different sizes of QD samples immediately following synthesis and after 3 months of storage in air. The peak positions remain the same with no increase in HWHM. Furthermore, we typically obtain photoluminescence quantum yields in the range of 30–60% for several months after synthesis and without storage in air free environments. Notably, we have measured quantum yield of 60% for QDs which had been in air for 5 months. This exceptional air stability has been observed in previous studies, and it is believed to be a result of nanocrystal surface passivation by chloride ions.<sup>15,16,37</sup> This property is unique to recipes using  $\text{PbCl}_2$  as a precursor, as it has been found that only small nanocrystals are air stable when synthesized via the Hines and Scholes method (which uses lead

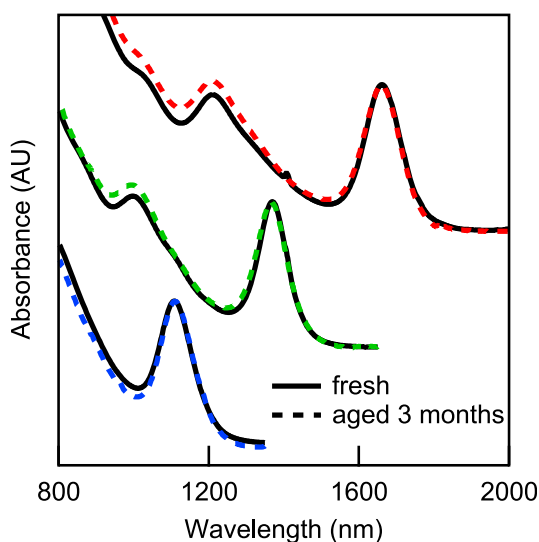


**Figure 8.** Absorption spectra for 4.7, 5.9, and 7.4 nm diameter PbS QDs before and after storage in air. The black solid lines are spectra taken immediately after synthesis, whereas the dashed colored lines are after the QDs have been stored dry and under ambient conditions for 3 months. For all sizes, the peak positions and HWHM are maintained.

oxide as the lead precursor).<sup>38,39</sup> Indeed, we also attribute the air stability shown here to chloride surface passivation, as observed via X-ray photoelectron spectroscopy (XPS) (see Figure S12). We first used XRD to ensure our QDs were well purified and there were no traces of crystalline  $\text{PbCl}_2$ . Using XPS, we still observe signal from chlorine, which supports the conclusion that the nanocrystals are passivated by a chloride layer.

A significant benefit of monodisperse QDs is their ability to self-assemble into two or three-dimensional ordered structures, which increases packing density and has the potential to improve transport properties in thin films.<sup>9,40–42</sup> In Figure 9a,b, we show TEM micrographs of two and three-dimensional ordering. Samples were prepared by drop casting QD suspensions in hexane onto TEM grids. The monolayer in Figure 9a self-assembled into a hexagonally close packed arrangement. Drop casting a more concentrated suspension of QDs yielded three-dimensional superlattices, such as that shown in Figure 9b. We estimate that this superlattice is approximately 5 QD layers thick, based on TEM contrast as compared to the monolayer. The high degree of monodispersity also allows for self-assembly of macro scale superlattices. In Figure 9c, we present the grazing-incidence small-angle X-ray scattering (GISAXS) pattern from a PbS QD film, which was formed by drop casting a 50 mg/mL suspension in toluene onto a silicon wafer. The area of the film measured by GISAXS was  $\sim 1 \text{ mm}^2$ . The sharply defined peaks indicate that this is a single crystal superlattice and the peak locations are consistent with body-centered cubic packing. Furthermore, the wide-angle X-ray scattering

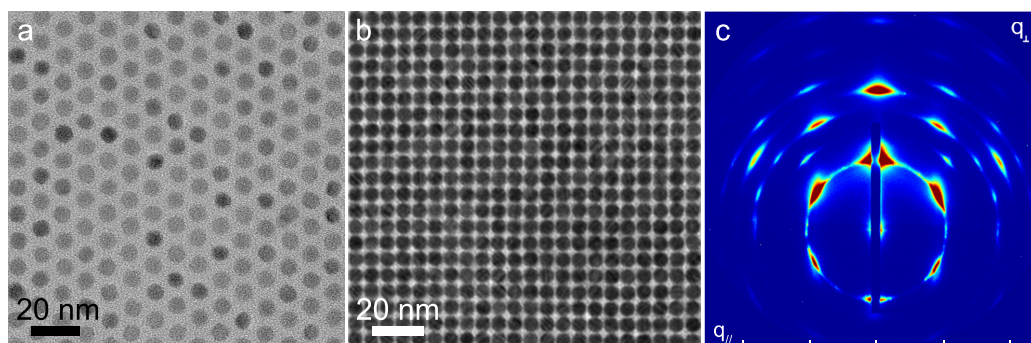


**Figure 9.** Two and three-dimensional self-assembly of PbS QDs. The TEM image in (a) of a QD monolayer shows near ideal hexagonal close packing. The TEM image in (b) shows a three-dimensional superlattice approximately 5 layers thick. Scale bars are 20 nm. GISAXS pattern in (c) shows long-range ordering in a body-centered cubic superlattice. The in-plane and out-of-plane scattering vectors are denoted, with tick increments of  $0.1 \text{ \AA}^{-1}$ .

shows that the atomic lattices of the nanocrystals are aligned as well (see Figure S13). These two observations are consistent with previous findings for PbS QDs which have been handled in air.<sup>43</sup>

## CONCLUSIONS

We have shown that Pb:S precursor stoichiometry is a critical parameter affecting the absorption line width of PbS QDs. When we employ a 24:1 Pb:S precursor stoichiometry ratio, it is possible to synthesize monodisperse PbS QDs with peak absorption

over a range of 1000–1800 nm (1.25–0.70 eV) and size dispersities of 3–5%. The QDs synthesized have tunable infrared emission with small Stokes shifts and quantum yields of 30–60%. We observed that the QDs are air-stable for several months and that they readily self-assemble into ordered lattices. We have developed a method to quickly and effectively remove excess precursor materials such that purification can be completed within 24 h of synthesis. Such QDs may be useful for photovoltaics, optoelectronics, and fundamental studies of QD photophysics.

## METHODS

**Synthesis.** Lead(II) chloride (Alfa Aesar, 99.999%), sulfur (Sigma-Aldrich,  $\geq 99.99\%$ ), oleylamine (Acros Organics, 80–90%), and oleic acid (Sigma-Aldrich, 90%) were used without further purification. The synthesis method studied here is a modified version of that first developed by Cademartiri *et al.*<sup>15</sup> and later studied by Moreels *et al.*<sup>16</sup> Please see the Supporting Information for a detailed description of the synthesis. Briefly, 0.040 g of sulfur was added to 7.5 mL of oleylamine in a one neck flask. This flask was heated to 120 °C in an oil bath for 20 min with nitrogen bubbling through the solution. The sulfur solution was then allowed to cool to room temperature, maintaining the nitrogen bubbling. The lead solution was prepared in a three neck flask by adding 2.50 g of  $\text{PbCl}_2$  to 7.5 mL of oleylamine. On a Schlenk line, the flask was degassed for 10 min to a pressure of  $\sim 150$  mTorr. It was then heated under nitrogen to 120 °C. At this point, the temperature was adjusted to the desired injection/growth temperature of 40, 80, or 120 °C. Subsequently, 2.25 mL of the sulfur solution was swiftly injected, resulting in a nucleation burst as evidenced by the solution turning black in color. This reaction stoichiometry is 9 mmol Pb and 0.375 mmol of S, a 24:1 precursor ratio. To access the other ratios studied here, the amount of  $\text{PbCl}_2$  was changed while keeping sulfur the same. To quench the reaction, the three neck cell was immersed in a water bath and 20 mL of cold hexanes was injected into the flask. This procedure typically yields  $\sim 75$  mg of purified QDs.

We find the recipe is amenable to scale-up, and we have been successful so far in scaling as much as  $10\times$  to yield  $\sim 750$  mg of product. In scaling up, we find the swiftness of the sulfur injection to be critical for replicating the growth kinetics observed in smaller batches. Therefore, we recommend concentrating the necessary sulfur in small volumes of oleylamine ( $\sim 5$  mL) rather than injecting the larger volumes required with a strictly linear scaling.

**Purification/Ligand Exchange.** After synthesis, QDs were purified to remove excess unreacted precursors and solvent. This involved precipitating the QDs using antisolvents followed by centrifugation. The two methods used for purification—with alcohols and with oleic acid—are discussed in detail in the Supporting Information. In all cases, the oleylamine ligands native to the QDs were exchanged for oleic acid ligands to improve colloidal stability.<sup>16</sup>

It is important to note that we were careful to always precipitate all of the PbS QDs from solution during purification, such that the supernate is either colorless or orange (from unreacted sulfur). This way we are not influencing the observed monodispersity by performing size-selective precipitations.

**Characterization.** Absorption spectra were measured using a Cary 5000 UV–vis-NIR spectrophotometer. The QDs were suspended in tetrachloroethylene for these measurements.

Photoluminescence spectra and photoluminescence lifetime measurements were performed using an InGaAs/InP single-photon counter from Micro Photon Devices. Infrared emission from the QDs was focused into a spectrograph (Acton 2500, Princeton Instruments) for the photoluminescence spectra measurements. Solution phase measurements were conducted with samples dispersed in tetrachloroethylene and were stirred for the duration of the measurement. Thin film samples were prepared by drop casting a concentrated solution onto glass microscope slides. The samples were excited by a 405 nm laser operating in either continuous wave mode for photoluminescence spectra or in pulsed mode (100 kHz repetition rate) for photoluminescence lifetime measurements. In all cases, the laser fluence was kept below  $5 \mu\text{J}/\text{cm}^2$ .

Photoluminescence quantum yield was measured using an integrating sphere (Labsphere). The QDs were suspended in tetrachloroethylene and excited with a 785 nm laser. Their emission was detected using an infrared photodiode (Newport 818-IR).

Transmission electron microscopy (TEM) was performed on a JEOL 2011 operating at 200 kV and using an objective aperture to increase mass–thickness contrast. Image analysis to determine average particle size and dispersity was done with the freely available software ImageJ. High-resolution TEM (HRTEM) images were taken on a JEOL 2010F operating at 200 kV. Samples were prepared by drop casting QD suspensions in hexane onto TEM grids coated with an amorphous carbon support film.

Energy-dispersive X-ray spectroscopy (EDS) was performed using a JEOL 2010 transmission electron microscope operating at 200 kV and equipped with an INCA detection system.

Small-angle X-ray scattering (SAXS) was measured on a Rigaku Smartlab with Cu K $\alpha$  source operating at 45 kV and 200 mA. Samples were prepared by filling glass capillaries with suspensions of QDs in toluene at concentrations of  $\sim$ 25 mg/mL. The instrument was configured using transmission mode geometry and parallel beam optics. The experimental SAXS data were fit using Rigaku NANO-Solver software to model the form factor of spherical PbS nanocrystals in a matrix of toluene. The background scattering from a pure toluene capillary was subtracted from the experimental data. The software also accounted for instrumental smearing.

Grazing-incidence small-angle X-ray scattering (GISAXS) and wide-angle X-ray scattering (WAXS) were performed at the undulator-based X9 beamline at the National Synchrotron Light Source at Brookhaven National Laboratory. The X-ray energy was set to 13.5 keV (wavelength 0.0918 nm), and the beam size was focused to 50  $\mu$ m tall by 100  $\mu$ m wide at the sample position using a KB mirror system. Due to the grazing-incidence, beam projection along the beam direction was  $\sim$ 1 cm. The grazing-incident angle of the X-ray beam was varied from 0.08° to 0.3°. The presented results are for 0.2°, which were found to be representative. 2D scattering data was collected on CCD detectors which were calibrated using a silver behenate standard. QD films were deposited on single crystalline silicon wafers.

X-ray diffraction (XRD) was performed on a Rigaku Smartlab with Cu K $\alpha$  source operating at 45 kV and 200 mA. Samples were prepared by drop casting a concentrated suspension of QDs in hexane onto a zero-background holder and allowing the solvent to evaporate.

X-ray photoelectron spectroscopy (XPS) spectra were collected using a PHI Versaprobe II equipped with a multichannel hemispherical analyzer and a monochromatic aluminum anode X-ray source operating at 100 W with a 100  $\mu$ m beam scanned over a 1.4 mm line across the sample surface. A dual-beam charge neutralization system was used with an electron neutralizer bias of 1.2 eV and an argon ion beam energy of 10 eV.

**Conflict of Interest:** The authors declare no competing financial interest.

**Supporting Information Available:** Detailed synthesis and purification methods, additional sulfur injection results, growth curves (peak wavelength, QD diameter, and HWHM evolution with time), photoluminescence HWHM, TEM size dispersity, TEM and SAXS analysis techniques, XRD, XPS, WAXS, EDS, sizing curve data and equations, and HWHM data table. This material is available free of charge via the Internet at <http://pubs.acs.org>.

**Acknowledgment.** The authors wish to thank S. Hunt for performing the XPS measurements, K. Yager for assistance with GISAXS and WAXS measurements, J. Scherer for assistance with quantum yield measurements, and N. Bertone of Micro Photon Devices, Inc., for use of the InGaAs/InP single photon detector. We also wish to thank D.-K. Ko, I. Moreels, B. Walker, and D. Wanger for helpful discussions. This work was primarily supported by the U.S. Department of Energy, Office of Basic Energy Sciences, under Award Number DE-SC0010538. M.C.W. was supported by a National Science Foundation Graduate Research Fellowship under Grant No. 1122374. TEM, XRD, XPS, and SAXS measurements were performed in the MRSEC Shared Experimental Facilities at MIT, supported by the National Science Foundation under award number DMR-08-19762.

GISAXS and WAXS measurements were performed at the Center for Functional Nanomaterials and the National Synchrotron Light Source, Brookhaven National Laboratory, which is supported by the U.S. Department of Energy, Office of Basic Energy Sciences, under Contract No. DE-AC02-98CH10886.

## REFERENCES AND NOTES

- Ip, A. H.; Thon, S. M.; Hoogland, S.; Voznyy, O.; Zhitomirsky, D.; Debnath, R.; Levina, L.; Rollny, L. R.; Carey, G. H.; Fischer, A.; *et al.* Hybrid Passivated Colloidal Quantum Dot Solids. *Nat. Nanotechnol.* **2012**, *7*, 577–582.
- Lunt, R. R.; Osedach, T. P.; Brown, P. R.; Rowehl, J. A.; Bulović, V. Practical Roadmap and Limits to Nanostructured Photovoltaics. *Adv. Mater.* **2011**, *23*, 5712–5727.
- Talapin, D. V.; Lee, J.-S.; Kovalenko, M. V.; Shevchenko, E. V. Prospects of Colloidal Nanocrystals for Electronic and Optoelectronic Applications. *Chem. Rev.* **2010**, *110*, 389–458.
- Konstantatos, G.; Howard, I.; Fischer, A.; Hoogland, S.; Clifford, J.; Klem, E.; Levina, L.; Sargent, E. H. Ultrasensitive Solution-Cast Quantum Dot Photodetectors. *Nature* **2006**, *442*, 180–183.
- Sun, L.; Choi, J. J.; Stachnik, D.; Bartnik, A. C.; Hyun, B.-R.; Malliaras, G. G.; Hanrath, T.; Wise, F. W. Bright Infrared Quantum-Dot Light-Emitting Diodes through Inter-Dot Spacing Control. *Nat. Nanotechnol.* **2012**, *7*, 369–373.
- Guyot-Sionnest, P. Electrical Transport in Colloidal Quantum Dot Films. *J. Phys. Chem. Lett.* **2012**, *3*, 1169–1175.
- Zhitomirsky, D.; Kramer, I. J.; Labelle, A. J.; Fischer, A.; Debnath, R.; Pan, J.; Bakr, O. M.; Sargent, E. H. Colloidal Quantum Dot Photovoltaics: The Effect of Polydispersity. *Nano Lett.* **2012**, *12*, 1007–1012.
- Murray, C. B.; Kagan, C. R.; Bawendi, M. G. Synthesis and Characterization of Monodisperse Nanocrystals and Close-Packed Nanocrystal Assemblies. *Annu. Rev. Mater. Sci.* **2000**, *30*, 545–610.
- Hanrath, T. Colloidal Nanocrystal Quantum Dot Assemblies as Artificial Solids. *J. Vac. Sci. Technol., A* **2012**, *30*, 030802.
- Shabaev, A.; Efros, A. L.; Efros, A. L. Dark and Photo-Conductivity in Ordered Array of Nanocrystals. *Nano Lett.* **2013**, *13*, 5454–5461.
- Steckel, J. S.; Colby, R.; Liu, W.; Hutchinson, K.; Breen, C.; Ritter, J.; Coe-Sullivan, S. Quantum Dot Manufacturing Requirements for the High Volume LCD Market. *SID Symp. Dig. Tech. Pap.* **2013**, *44*, 943–945.
- Semonin, O. E.; Luther, J. M.; Choi, S.; Chen, H.-Y.; Gao, J.; Nozik, A. J.; Beard, M. C. Peak External Photocurrent Quantum Efficiency Exceeding 100% via MEG in a Quantum Dot Solar Cell. *Science* **2011**, *334*, 1530–1533.
- Tisdale, W. A.; Williams, K. J.; Timp, B. A.; Norris, D. J.; Aydi, E. S.; Zhu, X.-Y. Hot-Electron Transfer from Semiconductor Nanocrystals. *Science* **2010**, *328*, 1543–1547.
- Hines, M. A.; Scholes, G. D. Colloidal PbS Nanocrystals with Size-Tunable Near-Infrared Emission: Observation of Post-Synthesis Self-Narrowing of the Particle Size Distribution. *Adv. Mater.* **2003**, *15*, 1844–1849.
- Cademartiri, L.; Bertolotti, J.; Sapienza, R.; Wiersma, D. S.; von Freymann, G.; Ozin, G. A. Multigram Scale, Solventless, and Diffusion-Controlled Route to Highly Monodisperse PbS Nanocrystals. *J. Phys. Chem. B* **2006**, *110*, 671–673.
- Moreels, I.; Justo, Y.; De Geyter, B.; Hastraete, K.; Martins, J. C.; Hens, Z. Size-Tunable, Bright, and Stable PbS Quantum Dots: A Surface Chemistry Study. *ACS Nano* **2011**, *5*, 2004–2012.
- Murray, C. B.; Norris, D. J.; Bawendi, M. G. Synthesis and Characterization of Nearly Monodisperse CdE (E = S, Se, Te) Semiconductor Nanocrystallites. *J. Am. Chem. Soc.* **1993**, *115*, 8706–8715.
- Chen, O.; Zhao, J.; Chauhan, V. P.; Cui, J.; Wong, C.; Harris, D. K.; Wei, H.; Han, H.-S.; Fukumura, D.; Jain, R. K.; *et al.* Compact High-Quality CdSe–CdS Core-Shell Nanocrystals with Narrow Emission Linewidths and Suppressed Blinking. *Nat. Mater.* **2013**, *12*, 445–451.



19. Peng, Z. A.; Peng, X. Formation of High-Quality CdTe, CdSe, and CdS Nanocrystals Using CdO as Precursor. *J. Am. Chem. Soc.* **2001**, *123*, 183–184.
20. Abe, S.; Čapek, R. K.; De Geyter, B.; Hens, Z. Tuning the Postfocused Size of Colloidal Nanocrystals by the Reaction Rate: From Theory to Application. *ACS Nano* **2012**, *6*, 42–53.
21. Talapin, D. V.; Rogach, A. L.; Kornowski, A.; Haase, M.; Weller, H. Highly Luminescent Monodisperse CdSe and CdSe/ZnS Nanocrystals Synthesized in a Hexadecylamine–Trioctylphosphine Oxide–Trioctylphosphine Mixture. *Nano Lett.* **2001**, *1*, 207–211.
22. Murray, C. B.; Sun, S.; Gaschler, W.; Doyle, H.; Betley, T. A.; Kagan, C. R. Colloidal Synthesis of Nanocrystals and Nanocrystal Superlattices. *IBM J. Res. Dev.* **2001**, *45*, 47–56.
23. Wehrenberg, B. L.; Wang, C.; Guyot-Sionnest, P. Interband and Intraband Optical Studies of PbSe Colloidal Quantum Dots. *J. Phys. Chem. B* **2002**, *106*, 10634–10640.
24. Du, H.; Chen, C.; Krishnan, R.; Krauss, T. D.; Harbold, J. M.; Wise, F. W.; Thomas, M. G.; Silcox, J. Optical Properties of Colloidal PbSe Nanocrystals. *Nano Lett.* **2002**, *2*, 1321–1324.
25. Yu, W. W.; Falkner, J. C.; Shih, B. S.; Colvin, V. L. Preparation and Characterization of Monodisperse PbSe Semiconductor Nanocrystals in a Noncoordinating Solvent. *Chem. Mater.* **2004**, *16*, 3318–3322.
26. Wadia, C.; Alivisatos, A. P.; Kammen, D. M. Materials Availability Expands the Opportunity for Large-Scale Photovoltaics Deployment. *Environ. Sci. Technol.* **2009**, *43*, 2072–2077.
27. Thon, S. M.; Ip, A. H.; Voznyy, O.; Levina, L.; Kemp, K. W.; Carey, G. H.; Masala, S.; Sargent, E. H. Role of Bond Adaptability in the Passivation of Colloidal Quantum Dot Solids. *ACS Nano* **2013**, *7*, 7680–7688.
28. Brown, P. R.; Lunt, R. R.; Zhao, N.; Osedach, T. P.; Wanger, D. D.; Chang, L.-Y.; Bawendi, M. G.; Bulović, V. Improved Current Extraction from ZnO/PbS Quantum Dot Heterojunction Photovoltaics Using a MoO<sub>3</sub> Interfacial Layer. *Nano Lett.* **2011**, *11*, 2955–2961.
29. Talapin, D. V.; Rogach, A. L.; Haase, M.; Weller, H. Evolution of an Ensemble of Nanoparticles in a Colloidal Solution: Theoretical Study. *J. Phys. Chem. B* **2001**, *105*, 12278–12285.
30. Peng, X.; Wickham, J.; Alivisatos, A. P. Kinetics of II–VI and III–V Colloidal Semiconductor Nanocrystal Growth: “Focusing” of Size Distributions. *J. Am. Chem. Soc.* **1998**, *120*, 5343–5344.
31. Cademartiri, L.; Ozin, G. A. Emerging Strategies for the Synthesis of Highly Monodisperse Colloidal Nanostructures. *Philos. Trans. R. Soc., A* **2010**, *368*, 4229–4248.
32. Cademartiri, L.; Montanari, E.; Calestani, G.; Migliori, A.; Guagliardi, A.; Ozin, G. A. Size-Dependent Extinction Coefficients of PbS Quantum Dots. *J. Am. Chem. Soc.* **2006**, *128*, 10337–10346.
33. Yuan, M.; Kemp, K. W.; Thon, S. M.; Kim, J. Y.; Chou, K. W.; Amassian, A.; Sargent, E. H. High-Performance Quantum-Dot Solids via Elemental Sulfur Synthesis. *Adv. Mater.* **2014**, DOI: 10.1002/adma.201305912.
34. Hassinen, A.; Moreels, I.; De Nolf, K.; Smet, P. F.; Martins, J. C.; Hens, Z. Short-Chain Alcohols Strip X-Type Ligands and Quench the Luminescence of PbSe and CdSe Quantum Dots, Acetonitrile Does Not. *J. Am. Chem. Soc.* **2012**, *134*, 20705–20712.
35. Akselrod, G. M.; Prins, F.; Poulikakos, L. V.; Lee, E. M. Y.; Weidman, M. C.; Mork, A. J.; Willard, A. P.; Bulovic, V.; Tisdale, W. A. Subdiffusive Exciton Transport in Quantum Dot Solids. *Nano Lett.* **2014**; DOI: 10.1021/nl501190s.
36. Choi, J. J.; Luria, J.; Hyun, B.-R.; Bartnik, A. C.; Sun, L.; Lim, Y.-F.; Marohn, J. a; Wise, F. W.; Hanrath, T. Photogenerated Exciton Dissociation in Highly Coupled Lead Salt Nanocrystal Assemblies. *Nano Lett.* **2010**, *10*, 1805–1811.
37. Cademartiri, L.; Ozin, G. A. Emerging Strategies for the Synthesis of Highly Monodisperse Colloidal Nanostructures. *Philos. Trans. R. Soc., A* **2010**, *368*, 4229–4248.
38. Tang, J.; Brzozowski, L.; Barkhouse, D. A. R.; Wang, X.; Debnath, R.; Wolowiec, R.; Palmiano, E.; Levina, L.; Pattantyus-Abraham, A. G.; Jamakosmanovic, D.; et al. Quantum Dot Photovoltaics in the Extreme Quantum Confinement Regime: The Surface-Chemical Origins of Exceptional Air- and Light-Stability. *ACS Nano* **2010**, *4*, 869–878.
39. Ihly, R.; Tolentino, J.; Liu, Y.; Gibbs, M.; Law, M. The Photo-thermal Stability of PbS Quantum Dot Solids. *ACS Nano* **2011**, *5*, 8175–8186.
40. Murray, C. B.; Kagan, C. R.; Bawendi, M. G. Self-Organization of CdSe Nanocrystallites into Three-Dimensional Quantum Dot Superlattices. *Science* **1995**, *270*, 1335–1338.
41. Dong, A.; Chen, J.; Vora, P. M.; Kikkawa, J. M.; Murray, C. B. Binary Nanocrystal Superlattice Membranes Self-Assembled at the Liquid-Air Interface. *Nature* **2010**, *466*, 474–477.
42. Shevchenko, E. V.; Talapin, D. V. Self-Assembly of Semiconductor Nanocrystals into Ordered Superstructures. *Semicond. Nanocryst. Quantum Dots* **2008**, 119–169.
43. Choi, J. J.; Bealing, C. R.; Bian, K.; Hughes, K. J.; Zhang, W.; Smilgies, D.-M.; Hennig, R. G.; Engstrom, J. R.; Hanrath, T. Controlling Nanocrystal Superlattice Symmetry and Shape-Anisotropic Interactions through Variable Ligand Surface Coverage. *J. Am. Chem. Soc.* **2011**, *133*, 3131–3138.